



Atomic-bridge structure in B-Co-P dual-active sites on boron nitride nanosheets for catalytic hydrogen generation

Huanhuan Zhang^{a,b}, Yanyan Liu^{a,c}, Huijuan Wei^b, Chengming Wang^b, Tao Liu^d, Xianli Wu^b, Saima Ashraf^b, Sehrish Mehdi^b, Shuyan Guan^a, Yanping Fan^a, Xinzheng Yue^b, Baozhong Liu^{a,e,**}, Yulong Zhang^{a,*}, Huaqiang Cao^{f,*}, Baojun Li^{a,b,f,**}

^a College of Chemistry and Chemical Engineering, Henan Polytechnic University, 2001 Century Avenue, Jiaozuo 454000, PR China

^b Research Center of Green Catalysis, College of Chemistry, College of Mechanical and Power Engineering, Zhengzhou University, 100 Science Road, Zhengzhou 450001, PR China

^c College of Science, Henan Agriculture University, 95 Wenhua Road, Zhengzhou 450002, PR China

^d CAS Key Laboratory for Biomedical Effects of Nanomaterials and Nanosafety, National Centre for Nanoscience and Technology, Beijing 100190, PR China

^e State Collaborative Innovation Center of Coal Work Safety and Clean-efficiency Utilization, Jiaozuo 454003, PR China

^f Department of Chemistry, Tsinghua University, Beijing 100084, PR China

ARTICLE INFO

Keywords:

Bimolecular activation
Borohydride hydrolysis
Heterointerface
Hexagonal boron nitride
Local P-inducing Strategy

ABSTRACT

Engineering the adsorption and dissociation of molecules on dual-active sites at interface is an integral constituent for rational design of high-efficient catalysts. Herein, we describe a unique atomic-bridge structure in B-Co-P (namely Co-B and Co-P) dual-active sites on boron nitride nanosheets to stimulate activity toward borohydride hydrolysis. The formation of atomic-bridge structure in B-Co-P dual-active sites is contributed to the Local P-inducing Strategy (LPIS). The catalyst exhibits superior kinetics (turnover frequency of 37 min^{-1}) with favorable stability during ammonia borane hydrolysis. Both experimental investigation and theoretical calculations reveal the key effects of atomic-bridge structure in B-Co-P interfacial dual-active sites on tailoring the electron density of Co species and reducing the energy barrier of reaction between ammonia borane and water molecules. This discovery is anticipated to furnish an impactful strategy to rationally design novel performance-oriented advanced catalysts for heterogeneous catalysis.

1. Introduction

Hydrogen is regarded as an attractive energy carrier due to its high gravimetric energy density and inherent cleanness [1,2]. Unfortunately, great challenges still exist in secure hydrogen storage and transportation [3,4]. Ammonia borane (NH_3BH_3) or sodium borohydride (NaBH_4) as valid chemical hydrogen-storage materials has significant applications for practical utilization [5,6]. Noble metals have promising in reducing the dissociation energy barrier of water and NH_3BH_3 molecules due to unique atomic orbitals and electronic properties [7]. High price and resource scarcity seriously limit their application [8,9]. Therefore, it is imperative to design high-performance non-noble metal catalysts to meet the requirement of sustainable development. Co or Ni has abundant coordination format and adjustable redox capability so that it presents the potential for construction of active structure [10,11]. The

unstable valence state of Co/Ni-based catalysts in process of borohydride hydrolysis leads a poor stability. Moreover, the lower activity and unclear catalytic mechanism in borohydride hydrolysis still remain challenges. Therefore, it is vital to design innovatively non-noble metal catalysts with highly efficient active structures.

Rational construction of dual-active sites at interface adjusts the electron configuration of components, optimizes the adsorption energy of reaction intermediates and boosts catalytic activity [12,13]. The design of controlled zero-valent Cu and univalent Cu active sites solves the corresponding thermodynamics/dynamics problems during electrocatalytic CO_2 reduction [14]. Hetero-diatom nickel-iron site and the orbital coupling between catalytic iron site and adjacent nickel atom boost electrochemical reduction [15]. The rational design of dual/-interface active site integrates the number of active sites, simultaneously modulates the electronic structure of catalysts and then boosts catalytic

* Corresponding authors.

** Corresponding authors at: College of Chemistry and Chemical Engineering, Henan Polytechnic University, 2001 Century Avenue, Jiaozuo 454000, PR China.

E-mail addresses: HPULiuking@163.com (B. Liu), zhangyulong@hpu.edu.cn (Y. Zhang), hqcao@mail.tsinghua.edu.cn (H. Cao), lbjcl@zzu.edu.cn (B. Li).

<https://doi.org/10.1016/j.apcatb.2022.121495>

Received 8 March 2022; Received in revised form 3 May 2022; Accepted 7 May 2022

Available online 11 May 2022

0926-3373/© 2022 Elsevier B.V. All rights reserved.

activity. However, dual-active sites with exposed interfaces are excavated purposely in order to further enhance the catalytic activity. Currently, atomic-bridge structures or other charge-transfer bridges on support play an importance role in improving catalytic activity via changing the electronic structure of bridging atoms and surface charge status of catalysts [16,17]. In order to further trigger catalytic activity of active structures, it is crucial to introduce active support to enhance the catalytic performance.

Metal-support interaction regulates the electronic structure of supported metal and leads to synergistic effects between metal and support, thus enhancing catalytic activity in heterogeneous catalysis [18,19]. The key to achieving homogeneity of active metal-oxide species on supports for highly controlled reactions is to construct a platform for designing adjustable catalysts to ensure uniform metal-support interactions. Hexagonal boron nitride (h-BN) as a 2D material consisting of alternating sp^2 -bonded boron and nitrogen atoms exhibits characteristic electron and band structure [20,21]. CuCo and CoNi NPs combined with h-BN present high catalytic activity during NH_3BH_3 hydrolysis due to chemical properties and electronic structure of metal NPs modified by h-BN [22,23]. Additionally, B-O/B-OH active sites formed in h-BN owing to reaction-induced presents excellent catalytic activity in oxidative dehydrogenation (ODH) reactions [24]. Furthermore, theoretical investigations affirm that interactions between metal atoms and h-BN surface defects prevent the aggregation of metal nanoparticles [25]. h-BN as an active constituent or inert support has promising power in the construction of dual-active sites [26,27]. Transition metal phosphides (TMPs) have emerged as important active materials due to adjustable hydroxyl or water molecules bonding ability [28]. Easy agglomeration caused by lattice stress release, one of the challenges in TMPs, destroys the original structure and reduces the catalytic activity [29]. Thus, to establish the correlation between dual-active sites and catalytic performance of catalysts through introducing active support is significant for heterogeneous catalysis.

Herein, atomic-bridge structure of B-Co-P is elaborately introduced in Co_3B -CoP/h-BN through partial substitution of P for B in Co_3B /h-BN by *LPIS*. The Co_3B -CoP/h-BN conveys optimal catalytic activity with a TOF of 37 min^{-1} towards NH_3BH_3 hydrolysis. Experimental and theoretical simulations confirm that the construction of Co-B and Co-P dual-active sites dramatically decreases the energy barrier for the activation of reactant molecules (NH_3BH_3 and H_2O) and thus promotes the bimolecular activation process. This research represents new insights into the design of cost-efficient catalysts for the field of heterogeneous catalysis.

2. Experimental section

2.1. Preparation of catalysts

Exfoliation of h-BN NSs: Purchased h-BN (0.5 g) was placed in quartz boat and heated at $800\text{ }^\circ\text{C}$ for 60 min in muffle furnace. Subsequently, the sample were dispersed in isopropanol (IPA), following stirring and ultrasonic for 5 h at an interval of 30 min. The above suspensions were centrifuged at 1500 rpm for 15 min. Then the obtain supernatant was treated by centrifugation at 10,000 rpm for 10 min. Finally, the exfoliated h-BN nanosheets were obtained after drying at $60\text{ }^\circ\text{C}$ in a vacuum oven.

Synthesis of Co_3B /h-BN: $CoCl_2 \cdot 6H_2O$ (714 mg) was added into H_2O (5 mL) and formed a uniform solution. The solution (5 mL) consist of polyvinylpyrrolidone (PVP, 500 mg) was added into the above-mentioned solution to form A solution. h-BN (75 mg) was dispersed in H_2O (20 mL) and IPA (20 mL) following stirring and ultrasonic for 2 h at an interval of 30 min (B solution). Subsequently, the B solution was added into the A solution and kept stirring for 1 h. Then, the solution of $NaBH_4$ (0.54 g, 20 mL H_2O) was added into the above solution under stirring. Finally, Co_3B /h-BN was harvested through centrifugation with water and ethanol following dried in a vacuum oven.

Synthesis of Co_3B -CoP/h-BN. Sodium hypophosphite (NaH_2PO_2 ,

200 mg) and Co_3B /h-BN (100 mg) were placed on the upstream and downstream sides of the tube furnace and heated to $300\text{ }^\circ\text{C}$ (heating rate: $3\text{ }^\circ\text{C min}^{-1}$, time: 2 h), then Co_3B -CoP/h-BN was obtained.

2.2. Hydrolysis of NH_3BH_3 and $NaBH_4$

Catalytic property of as-prepared catalysts during NH_3BH_3 hydrolysis was evaluated through a water-displacement method in lab-scale reactor. Details are presented in [Supporting Information](#).

2.3. Characterization

The crystalline phase of as-prepared samples was characterized through X-ray powder diffraction (XRD, Bruker/D8-Advance, $Cu-K\alpha$ radiation, $\lambda = 1.5418\text{ \AA}$) in the 2θ range from 5° to 80° . The morphology of materials was characterized through scanning electron microscope (SEM, Carl Zeiss NTS GmbH), transmission electron microscope (TEM, FEI Tecnai G² F20 S-TWIN electron microscope, operating at 200 kV). Details of characterizing the solid phase with X-ray absorption fine structure (XAFS) analyses for Co K-edge were performed with Si (111) crystal monochromators at the BL11B beamlines at the Shanghai Synchrotron Radiation Facility (SSRF) (Shanghai, China). Before the analysis at the beamline, samples were pressed into thin sheets with 1 cm in diameter and sealed using Kapton tape film. The XAFS spectra were recorded at room temperature using a 4-channel Silicon Drift Detector (SDD) Bruker 5040. Co K-edge extended X-ray absorption fine structure (EXAFS) spectra were recorded in transmission mode. Negligible changes in the line-shape and peak position of Co K-edge XANES spectra were observed between two scans taken for a specific sample. The XAFS spectra of these standard samples (Co Foil, and Co_3O_4) were recorded in transmission mode. The spectra were processed and analyzed by the software codes Athena and Artemis. X-ray photoelectron spectroscopy (XPS) was conducted on a Thermo Scientific K-Alpha spectrometer equipped with a monochromatic Al $K\alpha$ X-ray source (1486.6 eV) operating at 100 W. Samples were analyzed under vacuum ($P < 10^{-8}$ mbar) with a pass energy of 150 eV (survey scans) or 25 eV (high-resolution scans). All peaks would be calibrated with C 1 s peak binding energy at 284.8 eV for adventitious carbon. The experimental peaks were fitted with Avantage software. Raman spectra were obtained on Renishaw-in via Raman detection system using a 532 nm laser. Fourier transform infrared (FTIR) was conducted on Bruker Vertex 80 V in order to confirm the qualitative and quantitative analysis of materials. The active ingredients content (Cobalt element) in catalysts was calculated by inductively coupled plasma optical emission spectrometry (ICP-OES, Agilent 5110).

2.4. Computational details

The Vienna Ab Initio Package (VASP) was conducted to perform all the density functional theory (DFT) calculations within the generalized gradient approximation (GGA) using the Perdew-Burke-Ernzerhof (PBE) formulation. The projected augmented wave (PAW) potentials were applied to describe the ionic cores and take valence electrons into account using a plane wave basis set with a kinetic energy cutoff of 450 eV. Partial occupancies of the Kohn-Sham orbitals were allowed to use the Gaussian smearing method and a width of 0.05 eV. The electronic energy was considered self-consistent when the energy change was smaller than 10^{-4} eV. A geometry optimization was considered to be convergent when the force change was smaller than 0.05 eV/\AA . Grimme's DFT-D3 methodology was used to describe the dispersion interactions. The equilibrium lattice constants of bulk structures were optimized using a $3 \times 3 \times 2$ Monkhorst-Pack k-point grid for Brillouin zone sampling. The spin was set in our structures. Finally, the adsorption energies (E_{ads}) were calculated as:

$$E_{ads} = E_{ad/sub} - E_{ad} - E_{sub} \quad (1)$$

where $E_{ad/sub}$, E_{ad} , and E_{sub} are the total energies of the optimized adsorbate/substrate system, the adsorbate in the gas phase, and the clean substrate, respectively. The Brillouin zone integral uses the surfaces structures of $2 \times 2 \times 1$ monkhorst pack K point sampling for $Co_3B/h-BN$ and $Co_3B-CoP/h-BN$. The free energy (ΔG) for elemental reaction step was calculated as:

$$\Delta G = \Delta E + \Delta E_{ZPE} - T\Delta S \quad (2)$$

where ΔE is the difference between the total energy, ΔE_{ZPE} and ΔS are the differences in the zero-point energy and the change of entropy, T is the temperature ($T = 300$ K in this work), respectively. For the structure of $Co_3B-CoP/h-BN$, BN was fixed during calculating process.

Generally, energy convergence and force convergence exist in the calculation of structural optimization. The structural optimization is ended only after the co-operation of energy convergence and force convergence. The surface structure in this calculation system is complex due to the existence of BN and Co_3B-CoP heterostructure. Thus, the energy convergence of 10^{-4} eV [30] was conducted to make the structure has a rapid convergence and subsequently force convergence was operated further. Based on the above operation, although the energy convergence accuracy was 10^{-4} eV, the convergence accuracy of 10^{-6} eV was achieved actually on both the bulk phase and surface structure.

3. Results and discussion

3.1. Preparation and characterizations

The schematic illustration of atomic-bridge structure in B-Co-P (namely Co-B and Co-P) dual-active sites ($Co_3B-CoP/h-BN$) is depicted in Fig. 1a. First, h-BN was achieved by exfoliating bulk h-BN. $Co_3B/h-BN$ containing of Co-B active site was obtained through the one-step $NaBH_4$ reduction. Subsequently, the introduction of P element partially replaced the B element in Co_3B through *LPiS*, and then $Co_3B-CoP/h-BN$ was harvested. Illustratively, the exfoliative h-BN was an active support in the synthesis process and the B in $Co_3B-CoP/h-BN$ derived from the $NaBH_4$ reduction instead of the B element in h-BN. Fig. 1b is the diagram of the dual-active interface adjusted by Co_3B and CoP in $Co_3B-CoP/h-BN$ for boosting hydrogen generation during NH_3BH_3 hydrolysis.

TEM was employed to analyze local environment in catalysts. The exfoliative h-BN is detected as nanosheets with a size of 100 nm (Fig. 2a). The NPs in $Co_3B-CoP/h-BN$ has a uniform dispersion (Fig. 2b-d). The morphology of $Co_3B/h-BN$ has no obvious change with $Co_3B-CoP/h-BN$ (Fig. S1a, b). Co_3B without h-BN has serious aggregation (Fig. S1c, d). Fig. 2e is the structural model of $Co_3B-CoP/h-BN$. From HRTEM image of $Co_3B-CoP/h-BN$ (Fig. 2f), 0.203 and 0.205 nm are coherent to (210) and (022) planes of Co_3B , respectively. Moreover, 0.197 nm is corresponding to the (112) plane of CoP. The results confirm that the heterogeneous interface is formed and has the ability to construct the atomic-bridge structure of B-Co-P. The overlayers are observed on $Co_3B-CoP/h-BN$, demonstrating the importance of *LPiS* for

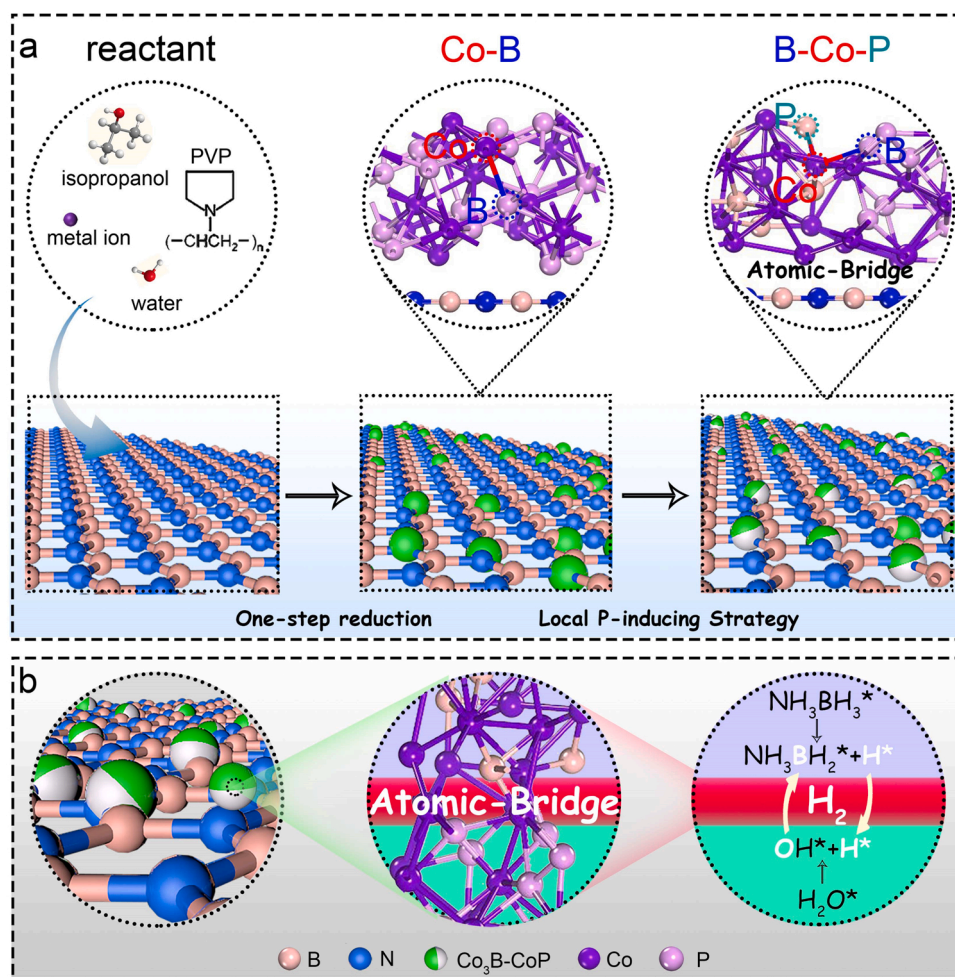


Fig. 1. (a) Schematic synthetic procedure of B-Co-P dual-active sites. (b) Schematic illustration of NH_3BH_3 and H_2O molecule adsorption, activation, dissociation and hydrogen generation processes on B-Co-P dual-active sites.

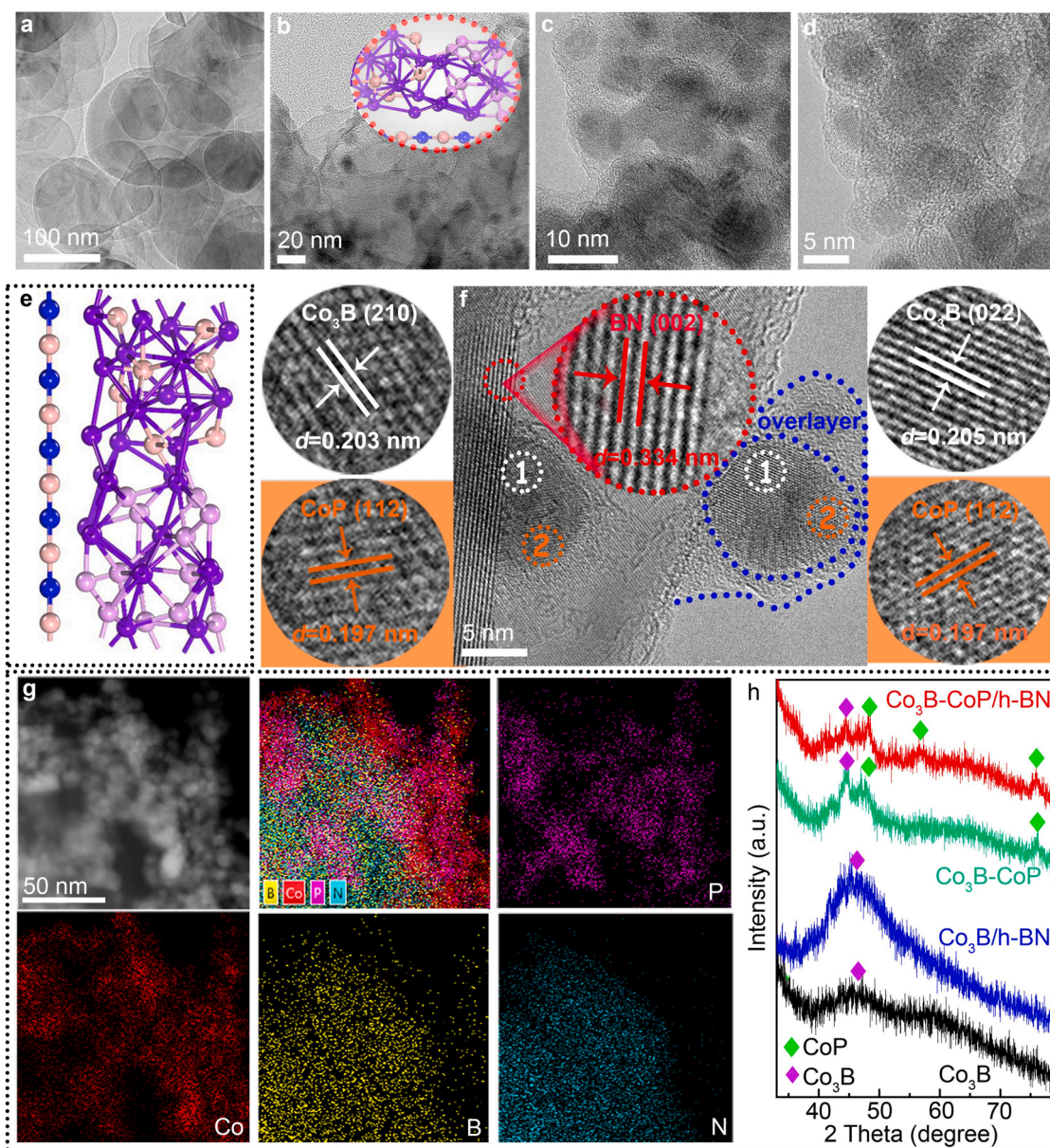


Fig. 2. TEM images of (a) exfoliated h-BN, (b-d) Co₃B-CoP/h-BN. (e) Structural model and (f) HRTEM images, (g) high-angle annular dark-field scanning transmission electron microscopy (HAADF-STEM) image and corresponding EDX-STEM element mapping images of Co₃B-CoP/h-BN. (h) XRD patterns of Co₃B, Co₃B-CoP, Co₃B/h-BN and Co₃B-CoP/h-BN.

the formation of the metal phosphides and migration of the support towards the active component [31]. The phenomenon can be explained by the competing processes of support migration and metal nanoparticle sintering at low temperature [32]. EDX-STEM element mapping images present dispersion uniformity of P, Co, B and N in Co₃B-CoP/h-BN (Fig. 2g). The structural and material composition of various sample is detected via XRD. The XRD patterns of h-BN before and after exfoliation are shown in Fig. S2. The peaks at 26.7°, 41.6°, 43.7°, 55.2°, 75.9° have perfect match with h-BN (JCPDS Card No. 34-0421) [33]. From Fig. 2h, peaks at 44.5° and 45.9° are indexed as (210) and (103) lattice facets of Co₃B (JCPDS Card No. 12-0443). Peaks at 48.1°, 56.8° and 75.9° are assigned to (211), (301) and (303) planes of CoP (JCPDS Card No. 29-0497) [34,35]. The XRD results confirm the existence of Co₃B and CoP and the heterostructure is constructed successfully.

XPS was conducted to investigate the valence state of elements in catalysts. The survey spectra confirm that elements P, Co, B, N exist in Co₃B/h-BN and Co₃B-CoP/h-BN (Fig. S3a). High resolution XPS

spectrum of P 2p in Co₃B-CoP/h-BN is shown in Fig. 3a. Peaks at 129.2 eV, 130.2 eV are assigned to P⁰ and 133.4 eV is assigned to oxidized P, respectively [36,37]. The results confirm the successful operation of LPiS and the growth of the atomic-bridge structure. In Co 2p spectrum of Co₃B-CoP/h-BN in Fig. 3b, peaks at 778.3 eV (Co 2p_{3/2}) and 793.8 eV (Co 2p_{1/2}) are ascribed to Co-P bonding in Co_xP. Peaks at 781.8 eV (Co 2p_{3/2}) and 798.3 eV (Co 2p_{1/2}) are endowed to partial oxidized bond due to partial oxidation of Co_xP in air. Peaks at 786.9 eV and 803.1 eV are assigned to shake-up satellite peaks [37,38]. In Co 2p spectrum of Co₃B/h-BN, peaks at 777.9 (Co 2p_{3/2}) and 792.6 eV (Co 2p_{1/2}) are corresponding to Co⁰, and peaks at 781.3 (Co 2p_{3/2}) and 796.8 eV (Co 2p_{1/2}) are corresponded to Co²⁺. Peaks at 787.0 eV, 803.1 eV are assigned to shake-up satellite peaks (Fig. 3b) [6,39]. In the high resolution XPS spectrum of B 1s in Co₃B-CoP/h-BN and Co₃B/h-BN, peaks at 190.5 eV, 191.3 eV are attributed to B-N and B-O band, respectively (Fig. 3c) [40]. The existence of B-O is caused by the reaction of NaBH₄ and the inevitable surface oxidation in these catalysts

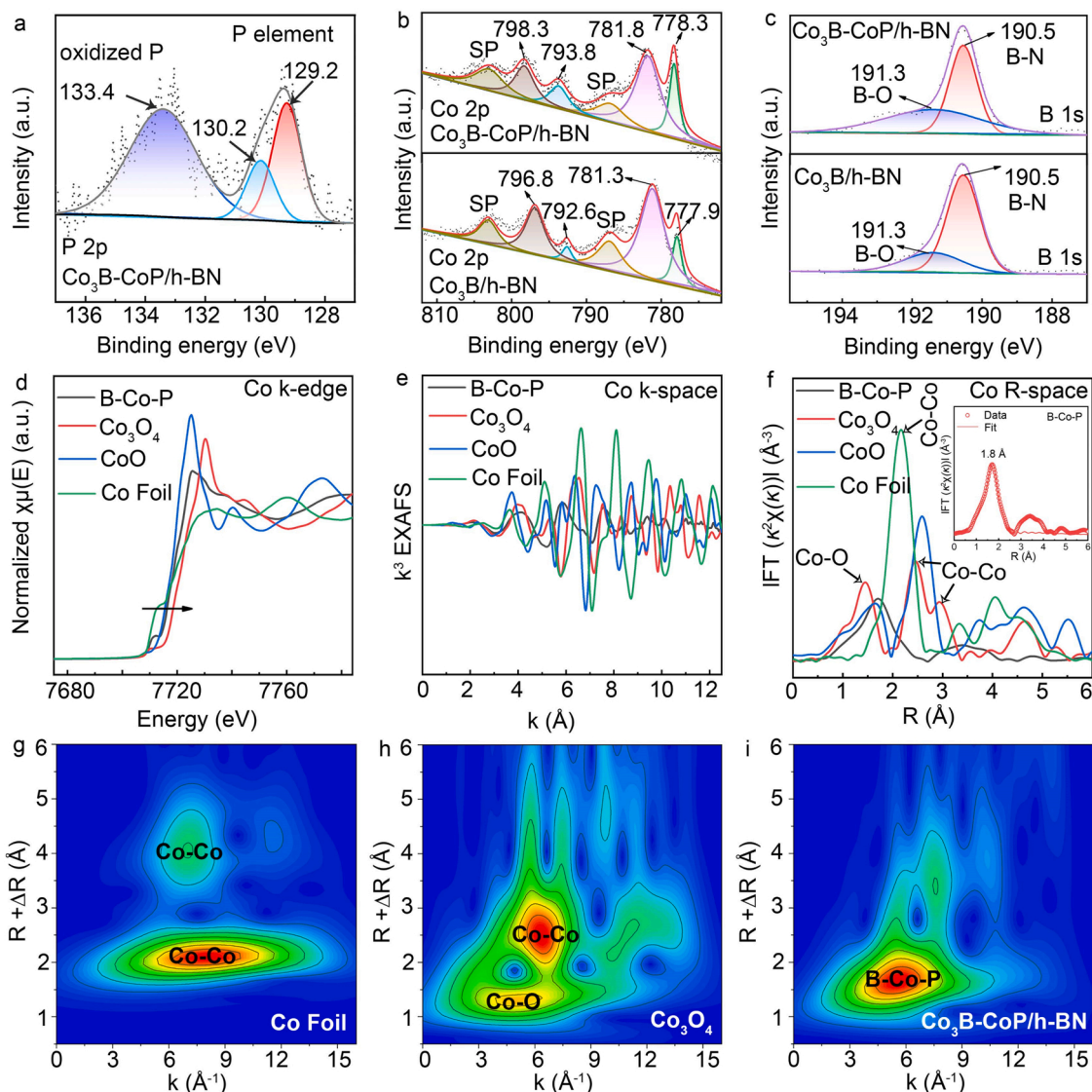


Fig. 3. High-resolution XPS spectra of (a) P 2p, (b) Co 2p, (c) B 1s in $\text{Co}_3\text{B-CoP/h-BN}$ and $\text{Co}_3\text{B/h-BN}$. (d) Co K-edge XANES spectra, (e) EXAFS spectra in k space and (f) Fourier transformation of the EXAFS spectra at R space of $\text{Co}_3\text{B-CoP/h-BN}$ (atomic-bridge structure in B-Co-P dual-active site), Co_3O_4 , CoO and Co Foil (the insert in Fig. 3f: corresponding EXAFS R space-fitting curves of B-Co-P in $\text{Co}_3\text{B-CoP/h-BN}$). (g-i) WT-EXAFS plot for Co Foil , Co_3O_4 and $\text{Co}_3\text{B-CoP/h-BN}$.

[41]. The N 1s peaks for $\text{Co}_3\text{B/h-BN}$ and $\text{Co}_3\text{B-CoP/h-BN}$ all contain N-B (398.2 eV), providing a perfect BN environment (Fig. S3b) [26]. The XRD and XPS results reveal that the formation of atomic-bridge structure and a strong electronic interaction existing in B-Co-P. The LPiS plays an important role in inducing the formation of atomic-bridge structure and dual-active site. Some element information from XPS is exhibited in Table S1.

FTIR and Raman spectra were used to detect chemical bond information between atomic-bridge structure and support. The intense absorptions at 1385 and 790 cm^{-1} in the FTIR spectra of h-BN, $\text{Co}_3\text{B/h-BN}$ and $\text{Co}_3\text{B-CoP/h-BN}$ are ascribed to the characteristic stretching ($\nu_{\text{B-N}}$) and bending mode ($\delta_{\text{B-N}}$) of sp^2 -hybridized h-BN skeleton, respectively [42]. The broad absorption band center located at 3410 cm^{-1} is indexed to the vibration of surface residual OH groups (Fig. S4a). The Raman peak located at 1370 cm^{-1} is attributed to the high frequency vibration ($\text{E}_{2\text{g}}$) of h-BN (analogous to the G peak in graphene) (Fig. S4b) [43]. The high frequency mode of $\text{E}_{2\text{g}}$ is due to B and N atoms moving against each other within a plane. The existence of h-BN enhances the charge transfer between B-Co-P dual-active site and h-BN. Then, the catalytic activity of the atomic-bridge structure is regulated through metal-support effect.

XAS was utilized to determine the valence states and coordination

environments of catalysts. From the Co K-edge XANES spectra, the absorption edges of $\text{Co}_3\text{B-CoP/h-BN}$ located between CoO foil and Co_3O_4 manifests the average positive valence approximate 2, in accordance with the XPS results (Fig. 3d) [44]. Thus, LPiS effectively reduces the valency of Co from a high oxidation state to a low oxidation state. Co Foil , CoO , Co_3O_4 and $\text{Co}_3\text{B-CoP/h-BN}$ show the similar structure feature in k space and the fluctuation curves of these samples mainly occur in the position of low 10, proving that there is no heavy metal in these samples (Fig. 3e) [45]. In the Fourier-transformed (FT) k^3 -weighted extended EXAFS spectra (Fig. 3f), the peak at 1.45 Å in the FT curve is attributed to Co-O scattering paths, and peaks at 2.16, 2.48, 2.95 Å are assigned to Co-Co scattering paths, respectively [46]. The FT EXAFS intensity of $\text{Co}_3\text{B-CoP/h-BN}$ (approximately 1.80 Å, adjacency to CoO) is significantly lower compared with Co foil and Co_3O_4 , demonstrating the rearrangement of the local atomic structure of Co via LPiS. Further fitting of the FT curve is operated in the R space of the first coordination shell to insight into the coordination structure of $\text{Co}_3\text{B-CoP/h-BN}$. The results show the single dominant FT (1.80 Å) peak corresponding to two types of coordination of Co-B (4.3) and Co-P (3.9) (inset in Fig. 3f and Table S2). This peak type tending to be Co-B and Co-P reveals the formation of an atomic-bridge structure with the operation of LPiS.

Based on the coordination number (approximately 4) of Co-B (4.3) and Co-P (3.9), typical Co-B4 and Co-P4 moieties predominate in Co₃B-CoP/h-BN. The special Co²⁺ coordination environment in Co₃B-CoP/h-BN is reflected by a particular path located at 1.8 Å. The perfect fitting on the EXAFS k and R space-fitting curves of Co₃B-CoP/h-BN, Co Foil and Co₃O₄ testifies the authenticity and reliability of these data (Figs. S5a-S5f). The specific bond lengths and coordination numbers of Co₃B-CoP/h-BN, Co Foil and Co₃O₄ are shown in Table S2. Additionally, wavelet transform (WT) EXAFS with high resolution in both k and R space is also performed (Fig. 3g-i). Corresponding WT signals of B-Co-P are visible in comparison with the Co-Co and Co-O for Co Foil and Co₃O₄. These results further demonstrate the existence of atomic-bridge structure in B-Co-P dual-active sites.

3.2. Catalytic kinetics evaluation

Some operations are conducted to investigate the catalytic kinetics evaluation of hydrogen generation of NH₃BH₃. The Co contents of Co₃B, Co₃B/h-BN, Co₃B-CoP, Co₃B-CoP/h-BN are determined by ICP-OES (Table S3). Fig. 4a is the catalytic hydrogen generation curves of various catalysts. The TOFs of Co₃B, Co₃B/h-BN, Co₃B-CoP, Co₃B-CoP/h-BN are calculated as 3, 8.6, 9.3, 37 min⁻¹, respectively (Fig. 4b). The

TOF (37 min⁻¹) of Co₃B-CoP/h-BN presents a rank top among non-precious metal phosphides based on h-BN under neutral reaction environment. The TOF values of reported catalysts based on cobalt or others phosphides are shown in Table S4. The above results unambiguously present that Co₃B-CoP/h-BN is the optimal catalyst due to the construction of interfacial active site of Co-B and Co-P. The construction of heterostructure accelerates electronic transfer, enhances the surface reaction kinetics, and further boosts the catalytic activity [47]. The TOF value on the optimal catalyst in presence of NaOH is up to 56 min⁻¹ (Fig. S6a, S6b). The enhanced performance is due to the pre-activation of atomic-bridge structure in B-Co-P dual-active site induced by alkaline environment provided by NaOH. This phenomenon confirms the role of co-catalyst of NaOH in B-Co-P dual-active site system. Furthermore, the effects of NaOH are discussed intensively in our previous researches [45,48].

Hydrogen generation at different temperatures are investigated on targeted catalyst to explore the effect of B-Co-P dual-active site on the E_a (Fig. 4c). The TOF of Co₃B-CoP/h-BN increased significantly from 27.5 min⁻¹ at 298 K to 72.3 min⁻¹ at 313 K (Fig. 4d). The triggering activity is due to the fast mass transformation caused by the higher temperature. The 51.8 kJ mol⁻¹ of E_a is obtained from the Eq. S2 (Fig. 4e). The E_a of other literatures are also listed in Table S3. Hydrogen

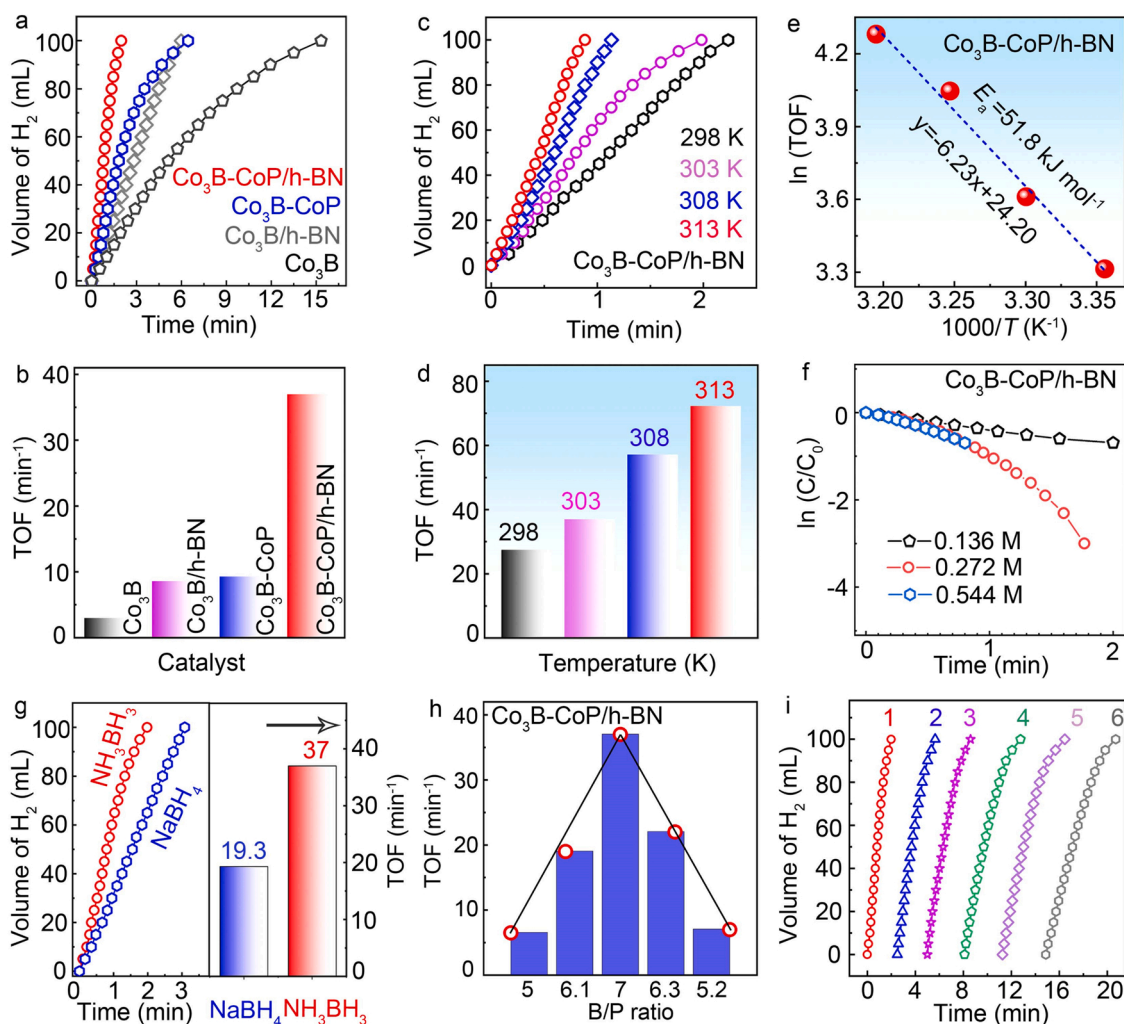


Fig. 4. (a) Hydrogen generation catalyzed by various catalysts. (b) Corresponding hydrogen generation activity (TOF, min⁻¹). (c, d) Hydrogen generation of Co₃B-CoP/h-BN at different temperature and corresponding hydrogen generation activity (TOF, min⁻¹). (e) The Arrhenius plot of ln(TOF) versus 1/T. (f) Curves of concentration changes vs time; C refers to the real-time concentration versus the reaction time and C₀ refers to the initial concentration. (g) Hydrogen generation of Co₃B-CoP/h-BN for NH₃BH₃, NaBH₄ and corresponding hydrogen generation activity (TOF, min⁻¹). (h) Hydrogen generation of different active component (the surface ratio of B and P active element) in Co₃B-CoP/h-BN. (i) Stability experiment of Co₃B-CoP/h-BN at 303 K.

generation on different NH_3BH_3 concentrations (0.136, 0.272, and 0.544 M) of $\text{Co}_3\text{B-CoP/h-BN}$ are also deliberated (Fig. S6c). The amount of generated hydrogen increases with an appropriate increase of NH_3BH_3 concentration. Additionally, a zero-order reaction is achieved from the curve of NH_3BH_3 concentration changes vs time during this reaction system (Fig. 4 f). The curve of NH_3BH_3 hydrolysis at different mass concentration of $\text{Co}_3\text{B-CoP/h-BN}$ in Fig. S6d confirms that the increased mass concentration presents an increased activity.

Hydrogen generation with NaBH_4 is proceeded under a similar method. A TOF of 19.3 min^{-1} is achieved (Fig. 4 g). Compared with NH_3BH_3 (37 min^{-1}), a decreased activity is emerged for NaBH_4 hydrolysis. This negative activity is attributed to the discrepant catalytic mechanism during borohydride hydrolysis caused by the different molecular geometry of NaBH_4 and NH_3BH_3 . Moreover, difference experiments of the amount of introduction of NaBH_4 (0.27, 0.41, 0.54, 0.81, 1.08 g) are operated in order to investigate the influence of different proportions of B, P element in $\text{Co}_3\text{B-CoP/h-BN}$. The surface ratio of B/P in $\text{Co}_3\text{B-CoP/h-BN}$ is expressed by XPS (Table S1). The corresponding catalytic activity and XPS results confirm that the 7 of B/P ratio in $\text{Co}_3\text{B-CoP/h-BN}$ presents the optimal catalytic performance (Fig. 4 h). In the stability experiment, the TOF values of $\text{Co}_3\text{B-CoP/h-BN}$ have a little decrease even after five cycles (Fig. 4 i). A series of characterizations of the used $\text{Co}_3\text{B-CoP/h-BN}$ are conducted and the results shown in Fig. S7. From XRD pattern in Fig. S7a, no noticeable change of composites is

observed between fresh or used $\text{Co}_3\text{B-CoP/h-BN}$. XPS spectra of the used $\text{Co}_3\text{B-CoP/h-BN}$ are analyzed and proved the presence of P, Co, B and N. The result illustrates the structure stability of $\text{Co}_3\text{B-CoP/h-BN}$ during hydrolysis system (Fig. S7b-S7e). The used $\text{Co}_3\text{B-CoP/h-BN}$ has a little conglomeration due to long-time employ (Fig. S7f). The SEM and quantitative EDS mapping images of the used $\text{Co}_3\text{B-CoP/h-BN}$ in Fig. S7g demonstrate the elements of P, Co, B, N have uniform dispersion on catalyst surface. These series characterizations confirm the stable existence of the atomic-bridge structure in dual-active sites after hydrolysis reaction.

3.3. Theoretical reflections on catalytic mechanism

DFT calculations were performed to identify the theoretical consideration on catalytic mechanism of B-Co-P dual-active sites. According to the NH_3BH_3 dehydrogenation mechanism, NH_3BH_3 (adsorbate) interacts with the active metal (adsorbent) on catalyst surface to form active intermediate species (adsorbed state). Then, the B-H bond is dissociated and the H radical is generated. The H radical combines with the other H radical derived from H_2O to generate H_2 . The adsorption energies (E_{ad}) of NH_3BH_3 on simulated catalysts are calculated by DFT. The E_{ad} values of NH_3BH_3 on the Co-P site and the Co-B site in $\text{Co}_3\text{B-CoP/h-BN}$ are calculated as 1.55 eV and 1.25 eV, respectively. Moreover, the B-H bond lengths in NH_3BH_3 on the Co-P site (1.498 Å) is

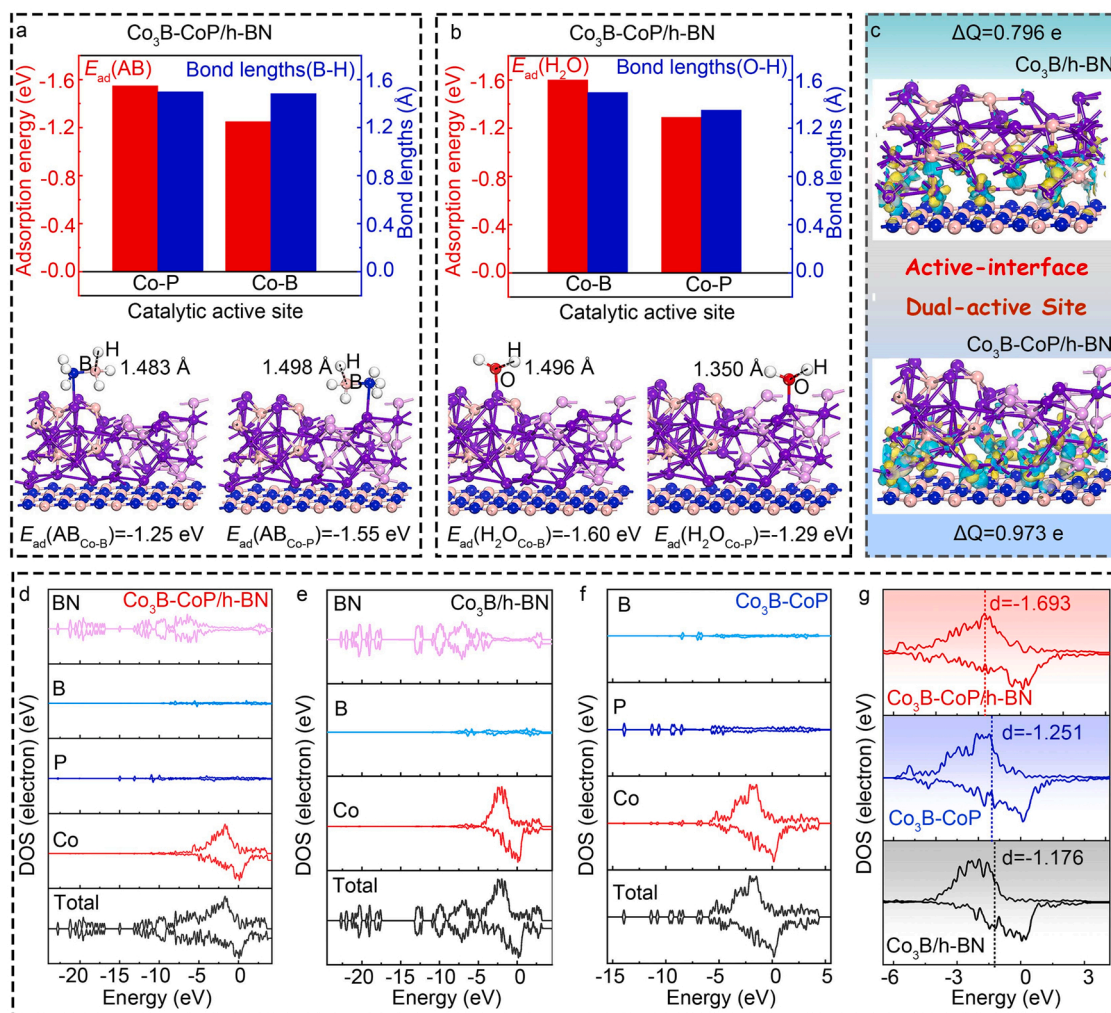


Fig. 5. (a, b) (Top) Adsorption energy of NH_3BH_3 and H_2O on Co-B site and Co-P site in $\text{Co}_3\text{B-CoP/h-BN}$ and corresponding B-H, O-H bond lengths in NH_3BH_3 and H_2O ; (Bottom) corresponding atomic models. (c) Atomic models with charge density difference of $\text{Co}_3\text{B/h-BN}$ and $\text{Co}_3\text{B-CoP/h-BN}$ (cyan region: charge accumulation; yellow region: charge depletion; with an iso-surface value of $0.03 \text{ eV}/\text{\AA}^3$). (d-f) DOS and (g) d-band center on the $\text{Co}_3\text{B-CoP/h-BN}$, $\text{Co}_3\text{B/h-BN}$ and $\text{Co}_3\text{B-CoP}$.

higher than the Co-B site (1.483 Å) in Co₃B-CoP/h-BN (Fig. 5a). These above results confirm that NH₃BH₃ is more easily adsorbed on the Co-P site in Co₃B-CoP/h-BN and the B-H bond in NH₃BH₃ have a potential weak bond energy. Coincidentally, the corresponding E_{ad} of H₂O on the Co-P site (1.29 eV) is lower than Co-B site (1.60 eV) in Co₃B-CoP/h-BN. Similarly, the O-H bond lengths in H₂O on the Co-P site (1.350 Å) is lower compared with Co-B site (1.496 Å) (Fig. 5b). These above results confirm that H₂O is more easily adsorbed on the Co-B site in Co₃B-CoP/h-BN and O-H bond in H₂O have a potential weak bond energy. The E_{ad} and bond length information of other contrastive catalysts are shown in Table S5. The weakening of B-H (O-H) bonds in NH₃BH₃ (H₂O) after

adsorption on the Co-P (Co-B) site in Co₃B-CoP/h-BN is conducive to the release of H radical and resist the broken of B-N bond, avoiding the production of unwanted byproducts [23]. This LPiS enhances the ability to weaken the bond energy of the reaction intermediate species through the atomic-bridge structure in B-Co-P dual-active sites and boosts catalytic activity [49].

Average Bader charge analysis further demonstrates a charge transfer of 0.796 e from active component (Co₃B) to h-BN and a charge transfer of 0.973 e from the active component (Co₃B-CoP) to h-BN after introducing P element. The phenomenon reveals that P modulation accelerates the electronic transfer of active ingredients and supports

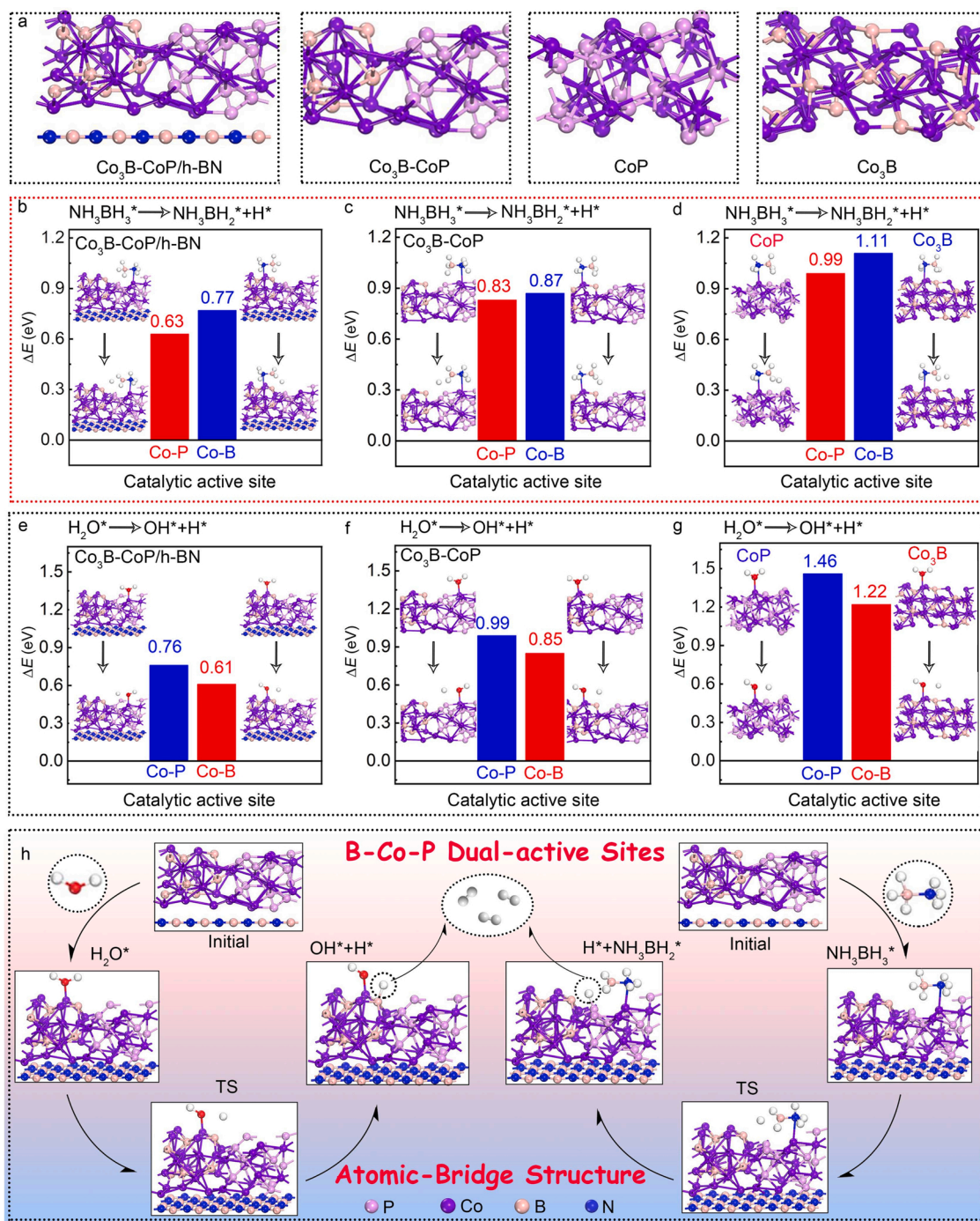


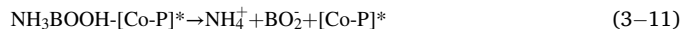
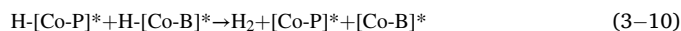
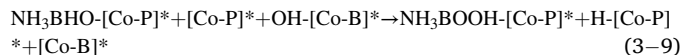
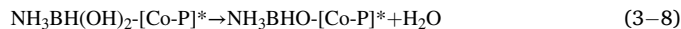
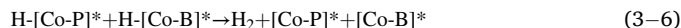
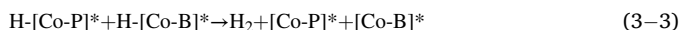
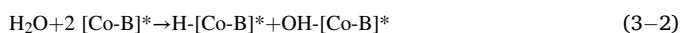
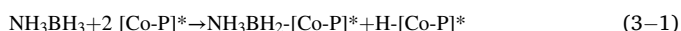
Fig. 6. (a) Optimized atomic model of Co₃B-CoP/h-BN, Co₃B-CoP, pristine Co₃B, pristine CoP. ΔE of NH₃BH₃ and H₂O dissociation on Co-B site, Co-P site of (b, e) Co₃B-CoP/h-BN, (c, f) Co₃B-CoP, and (d, g) pristine Co₃B, pristine CoP surface and corresponding optimized atomic structural model. (h) Proposed theoretical reflections on catalytic mechanism of Co₃B-CoP/h-BN for NH₃BH₃ hydrolysis.

(Fig. 5c). Charge transfer after the introduction of P is enhanced because of obvious decrease of work functions [46] (the larger difference of work function, the stronger tendency of electron transfer). Moreover, the density of states (DOS) of the active component on catalysts is also calculated. The total DOS of Co₃B-CoP/h-BN closed to the Fermi level apparently increases upon the introduction of P atoms compared with Co₃B/h-BN. The result interprets higher charge carrier density and favorable charge transfer in catalytic process of Co₃B-CoP/h-BN. Simultaneously, the DOS of Co element in Co₃B-CoP/h-BN closed to the Fermi level apparently decreases and the P element occurs compared with Co₃B/h-BN (Fig. 5d, e). The DOS of Co₃B-CoP/h-BN and Co₃B-CoP is also calculated and demonstrates that BN exists in target catalyst (Fig. 5f). The d-band center of Co₃B-CoP/h-BN (−1.693 eV) moves away from the Fermi level in comparison with pristine Co₃B-CoP (−1.251 eV) and Co₃B/h-BN (−1.176 eV), according with the d-band center theory (Fig. 5g) [49]. Noteworthy, electron density of d-band reduces following the reduction of d-band center. The phenomenon decreases the surface electrons that accept the electronic coordination of reaction molecules. The dramatic decrease of surface electrons is adverse to the adsorption/desorption of reaction molecules (NH₃BH₃ and H₂O) and further affects the intrinsic activity of catalysts. Therefore, medium chemical adsorption produced by suitable d-band center is responsible for superior activity.

Fig. 6a presents the atomic structure of various calculational catalysts. Catalytic reactions start with the adsorption of NH₃BH₃ and H₂O on atomic-bridge structure surface in B-Co-P dual-active sites. Subsequently, dissociation of NH₃BH₃ and H₂O occurs on atomic-bridge structure surface. Detailed reaction energy barrier (ΔE) bar charts of Co-B and Co-P active sites on Co₃B-CoP/h-BN, Co₃B-CoP, pristine Co₃B and pristine CoP are corroborated by DFT. In the perspective of kinetics, the ΔE of NH₃BH₃ dissociation on Co-P active site in Co₃B-CoP/h-BN ($\Delta E = 0.63$ eV) is lower than that on Co₃B-CoP ($\Delta E = 0.83$ eV) and pristine CoP ($\Delta E = 0.99$ eV). Analogously, the ΔE of NH₃BH₃ dissociation on Co-B active site conveys the optimal value in Co₃B-CoP/h-BN ($\Delta E = 0.77$ eV) compared with Co₃B-CoP ($\Delta E = 0.87$ eV) and pristine Co₃B ($\Delta E = 1.11$ eV). From the above results, Co₃B-CoP/h-BN has the optimal dissociation function for NH₃BH₃ molecule. The Co-P is more easily to activate NH₃BH₃ ($\Delta E = 0.63$ eV) compared with Co-B site ($\Delta E = 0.77$ eV) (Fig. 6b-d). The ΔE of H₂O dissociation on Co-P/Co-B active site in Co₃B-CoP/h-BN ($\Delta E = 0.76/0.61$ eV) is lower than those on Co₃B-CoP ($\Delta E = 0.99/0.85$ eV), pristine CoP ($\Delta E = 1.46$ eV), pristine Co₃B ($\Delta E = 1.22$ eV). The Co-B site is more easily to activate H₂O ($\Delta E = 0.61$ eV) compared with Co-P site ($\Delta E = 0.76$ eV) (Fig. 6e-g). In conclusion, Co₃B-CoP/h-BN presents favorable ability to activate NH₃BH₃ and H₂O molecule (Co-P site activates NH₃BH₃, Co-B site activates H₂O).

In situ Raman analysis is operated after the introduction of water molecules into catalysts (Fig. S8). Two peaks at about 3239 and 3410 cm^{−1} (water peaks) confirm water molecules are easy to dissociate [5,45]. The peaks intensity of water molecule on Co₃B-CoP/h-BN displays more optimistic than Co₃B/h-BN. This result confirms that LPiS enhances the ability of Co₃B-CoP/h-BN for the dissociation of water molecules. The construction of B-Co-P dual-active sites containing of Co-B and Co-P through LPiS modifies the catalysts surface structure. Thus, Co₃B-CoP/h-BN presents a reduced ΔE of the dissociation reaction and an enhanced hydrogen generation activity. Fig. 6h depicts the possible theoretical reflections on catalytic mechanism and details are as the following Eq. (3),

Path:



Firstly, NH₃BH₃, H₂O and Co₃B-CoP/h-BN are independent states. Subsequently, NH₃BH₃ and H₂O molecules are adsorbed on Co₃B-CoP/h-BN surface through the atomic-bridge structure in B-Co-P dual-active sites, respectively. Then, NH₃BH₃-[Co-P]^{*} and H₂O-[Co-B]^{*} are formed. H₂O-[Co-B]^{*} is more easy to dissociate into OH-[Co-B]^{*} and H-[Co-B]^{*}. The B-H bond in NH₃BH₃-[Co-P]^{*} is broken to form NH₃BH₂-[Co-P]^{*} and H-[Co-P]^{*}. Then, H-[Co-P]^{*} and H-[Co-B]^{*} generate a H₂ molecule released from the active-catalyst surface, along with the attack of OH-[Co-B]^{*} to NH₃BH₂-[Co-P]^{*} and the generation of NH₃BH₂OH^{*} [5,45,48]. The reaction continues until the other two H₂ molecules are generated according to the similar reaction path (Fig. 6h). In real heterogeneous catalysis, several steps are carried out at the same time via some multipoint interaction. The synchronous adsorption/dissociation of NH₃BH₃ and H₂O and the interaction in the complex intermediate contribute to the overall catalytic reaction and lead an easier kinetics for catalytic reaction. The B-Co-P dual-active sites induced by LPiS is responsible for the intrinsic catalytic activity of Co₃B-CoP/h-BN. In recent reports, a reverse spillover effect has been proposed for NiO/A-l₂O₃/Pt during NH₃BH₃ hydrolysis. This reverse spillover effects are more pronounced on precious metal catalysts [50]. It is noteworthy that cobalt phosphides have the chemical properties similar to precious metals. The reverse spillover effects may also exist in the non-precious Co₃B-CoP/h-BN catalyst. The contribution ratio of the reverse spillover effects is very weak and negligible. Generally, under the in-depth understanding of atomic-bridge structure in B-Co-P, the design of dual-active sites provides theoretical validation for the catalytic activities toward H₂ production.

4. Conclusions

In conclusion, the atomic-bridge structure in B-Co-P dual-active sites is successfully developed by a facile one-step reduction and Local P-inducing Strategy. This dual-active sites induce high catalytic activity during catalytic reaction. The optimal catalyst conveys the tremendous activity along with a top-ranked TOF of 37 min^{−1} among non-noble metal phosphides catalysts during borohydride hydrolysis. The stability in hydrogen generation remains no obvious loss. The superior catalytic activity is endowed to the construction of B-Co-P dual-active sites through the formation of atomic-bridge structure induced by LPiS. The B-Co-P dual-active sites with unique atomic-bridge structure are favorable for enhancing the activity and stability for NH₃BH₃ hydrolysis by tuning the electronic structure and chemical coordination environment of Co-B and Co-P active site. Thus, the B-Co-P dual-active sites present excellent ability for optimizing the adsorption and dissociation energies of ammonia borane and water molecules on atomic-bridge structure surface during catalytic reaction. This work paves a new ideology to modulate the dual-active sites and promote the fundamental researches in the structure-function-performance relationship.

CRedit authorship contribution statement

Huanhuan Zhang: Investigation, Visualization, Writing – original draft, Writing – review & editing, Formal analysis. **Yanyan Liu:**

Investigation, Visualization, Writing – review & editing, Formal analysis. **Huijuan Wei**: Investigation, Visualization, Formal analysis, The supporting of contribution. **Chengming Wang**: Formal analysis, the supporting of contribution. **Tao Liu**: Formal analysis, the supporting of contribution. **Xianli Wu**: Formal analysis, the supporting of contribution. **Saima Ashraf**: Formal analysis, the supporting of contribution. **Sehrish Mehdi**: formal analysis, the supporting of contribution. **Shuyan Guan**: Formal analysis, the supporting of contribution. **Yanping Fan**: Investigation, Visualization, Formal analysis, The supporting of contribution. **Xinzheng Yue**: Formal analysis, The supporting of contribution. **Baozhong Liu**: Project administration, Visualization, Funding acquisition, Formal analysis, Supervision, The supporting of contribution. **Yulong Zhang**: Visualization, Formal analysis, Supervision, The supporting of contribution. **Huaqiang Cao**: Visualization, Formal analysis, Supervision, The Supporting of contribution. **Baojun Li**: Visualization, Formal analysis, Supervision, Conceptualization, The lead of contribution.

Declaration of Competing Interest

The authors declare that they have no known competing financial interests or personal relationships that could have appeared to influence the work reported in this paper.

Acknowledgments

Financial supports from the National Natural Science Foundation of China (no. 52071135, 22075254, 51871090, U1804135, 21401168 and 51671080), Plan for Scientific Innovation Talent of Henan Province (no. 194200510019) and Key Project of Educational Commission of Henan Province (no. 19A150025) are acknowledged.

Appendix A. Supporting information

Supplementary data associated with this article can be found in the online version at [doi:10.1016/j.apcatb.2022.121495](https://doi.org/10.1016/j.apcatb.2022.121495).

References

- [1] P. Li, R. Chen, Y. Huang, W. Li, S. Zhao, S. Tian, Activating transition metal via synergistic anomalous phase and doping engineering towards enhanced dehydrogenation of ammonia borane, *Appl. Catal. B Environ.* 300 (2022), 120725.
- [2] X. Huang, Y. Liu, H. Wen, R. Shen, S. Mehdi, X. Wu, E. Liang, X. Guo, B. Li, Ensemble-boosting effect of Ru-Cu alloy on catalytic activity towards hydrogen evolution in ammonia borane hydrolysis, *Appl. Catal. B Environ.* 287 (2021), 119960.
- [3] J. Liu, X. Liu, H. Shi, J. Luo, L. Wang, J. Liang, S. Li, L. Yang, T. Wang, Y. Huang, Q. Li, Breaking the scaling relations of oxygen evolution reaction on amorphous NiFeP nanostructures with enhanced activity for overall seawater splitting, *Appl. Catal. B Environ.* 302 (2021), 120862.
- [4] Z. Peng, J. Liu, B. Hu, Y. Yang, Y. Guo, B. Li, L. Li, Z. Zhang, B. Cui, L. He, M. Du, Surface engineering on Nickel–Ruthenium nanoalloys attached defective carbon sites as superior bifunctional electrocatalysts for overall water splitting, *ACS Appl. Mater. Interfaces* 12 (2020) 13842–13851.
- [5] R. Shen, Y. Liu, H. Wen, X. Wu, G. Han, X. Yue, S. Mehdi, T. Liu, H. Cao, E. Liang, B. Li, Engineering bimodal oxygen vacancies and Pt to boost the activity toward water dissociation, *Small* 18 (2022), 2105588.
- [6] Y. Liu, G. Han, X. Zhang, C. Xing, C. Du, H. Cao, B. Li, Co-Co₃O₄@carbon core–shells derived from metal–organic framework nanocrystals as efficient hydrogen evolution catalysts, *Nano Res.* 10 (2017) 3035–3048.
- [7] S. Gong, W. Wang, C. Zhang, M. Zhu, R. Lu, J. Ye, H. Yang, C. Wu, J. Liu, D. Rao, S. Shao, X. Lv, Tuning the metal electronic structure of anchored cobalt phthalocyanine via dual-regulator for efficient CO₂ electroreduction and Zn-CO₂ batteries, *Adv. Funct. Mater.* (2022), 2110649.
- [8] Y. Liu, H. Wen, D. Zhou, X. Huang, X. Wu, J. Jiang, X. Guo, B. Li, Tuning surface d charge of Ni-Ru alloys for unprecedented catalytic activity towards hydrogen generation from ammonia borane hydrolysis, *Appl. Catal. B Environ.* 291 (2021), 120094.
- [9] J. Cai, J. Ding, D. Wei, X. Xie, B. Li, S. Lu, J. Zhang, Y. Liu, Q. Cai, S. Zang, Coupling of Ru and O-vacancy on 2D Mo-based electrocatalyst via a solid-phase interface reaction strategy for hydrogen evolution reaction, *Adv. Energy Mater.* 11 (2021), 2100141.
- [10] R. Zeng, Y. Yang, X. Feng, H. Li, L.M. Gibbs, F.J. DiSalvo, H.D. Abruna, Nonprecious transition metal nitrides as efficient oxygen reduction electrocatalysts for alkaline fuel cells, *Sci. Adv.* 8 (2022) eabj1584.
- [11] Z. Chen, G. Zhang, Y. Wen, N. Chen, W. Chen, T. Regier, J. Dynes, Y. Zheng, S. Sun, Atomically dispersed Fe-Co bimetallic catalysts for the promoted electroreduction of carbon dioxide, *Nano Micro Lett.* 14 (2022) 25.
- [12] Z. Xia, X. Chen, H. Ci, Z. Fan, Y. Yi, W. Yin, N. Wei, J. Cai, Y. Zhang, J. Sun, Designing N-doped graphene/ReSe₂/Ti₃C₂ MXene heterostructure frameworks as promising anodes for high-rate potassium-ion batteries, *J. Energy Chem.* 53 (2021) 155–162.
- [13] X. Li, J. Zhang, Y. Huo, K. Dai, S. Li, S. Chen, Two-dimensional sulfur- and chlorine-codoped g-C₃N₄/CdSe-amine heterostructures nanocomposite with effective interfacial charge transfer and mechanism insight, *Appl. Catal. B Environ.* 280 (2021), 119452.
- [14] X. Yuan, S. Chen, D. Cheng, L. Li, W. Zhu, D. Zhong, Z. Zhao, J. Li, T. Wang, J. Gong, Controllable Cu⁰-Cu⁺ sites for electrocatalytic reduction of carbon dioxide, *Angew. Chem. Int. Ed.* 60 (2021) 15344–15347.
- [15] Z. Zeng, L.Y. Gan, H. Bin Yang, X. Su, J. Gao, W. Liu, H. Matsumoto, J. Gong, J. Zhang, W. Cai, Z. Zhang, Y. Yan, B. Liu, P. Chen, Orbital coupling of hetero-diatom nickel-iron site for bifunctional electrocatalysis of CO₂ reduction and oxygen evolution, *Nat. Commun.* 12 (2021) 4088.
- [16] X. Cao, L. Zhao, B. Wulan, D. Tan, Q. Chen, J. Ma, J. Zhang, Atomic bridging structure of nickel–nitrogen–carbon for highly efficient electrocatalytic reduction of CO₂, *Angew. Chem. Int. Ed.* 61 (2021), e202113918.
- [17] P. Chen, B. Lei, X. Dong, H. Wang, J. Sheng, W. Cui, J. Li, Y. Sun, Z. Wang, F. Dong, Rare-earth single-atom La–N charge-transfer bridge on carbon nitride for highly efficient and selective photocatalytic CO₂ reduction, *ACS Nano* 14 (2020) 15841–15852.
- [18] D.G. Araiza, D.G. Arcos, A. Gómez-Cortés, G. Díaz, Dry reforming of methane over Pt–Ni/CeO₂ catalysts: Effect of the metal composition on the stability, *Catal. Today* 360 (2021) 46–54.
- [19] L.-P. Yuan, W.-J. Jiang, X.-L. Liu, Y.-H. He, C. He, T. Tang, J. Zhang, J.-S. Hu, Molecularly engineered strong metal oxide–support interaction enables highly efficient and stable CO₂ electroreduction, *ACS Catal.* 10 (2020) 13227.
- [20] L. He, H. Wang, L. Chen, X. Wang, H. Xie, C. Jiang, C. Li, K. Elibol, J. Meyer, K. Watanabe, T. Taniguchi, Z. Wu, W. Wang, Z. Ni, X. Miao, C. Zhang, D. Zhang, H. Wang, X. Xie, Isolating hydrogen in hexagonal boron nitride bubbles by a plasma treatment, *Nat. Commun.* 10 (2019) 2815.
- [21] S. Zhao, S. Yoo, S. Wang, B. Lyu, S. Kahn, F. Wu, Z. Zhao, D. Cui, W. Zhao, Y. Yoon, M.I.B. Utama, W. Shi, K. Watanabe, T. Taniguchi, M.F. Crommie, Z. Shi, C. Zhou, F. Wang, Tunneling spectroscopy in carbon nanotube–hexagonal boron nitride–carbon nanotube heterojunctions, *Nano Lett.* 20 (2020) 6712–6718.
- [22] X. Yang, Q. Li, J. Lin, X. Yang, C. Yu, Z. Liu, Y. Fang, Y. Huang, C. Tang, CuCo binary metal nanoparticles supported on boron nitride nanofibers as highly efficient catalysts for hydrogen generation from hydrolysis of ammonia borane, *J. Power Sources* 431 (2019) 135–143.
- [23] D. Fan, X. Lv, J. Feng, S. Zhang, J. Bai, R. Lu, J. Liu, Cobalt nickel nanoparticles encapsulated within hexagonal boron nitride as stable, catalytic dehydrogenation nanoreactor, *Int. J. Hydrog. Energy* 42 (2017) 11312–11320.
- [24] J. Dong, Q. Fu, H. Li, J. Xiao, B. Yang, B. Zhang, Y. Bai, T. Song, R. Zhang, L. Gao, J. Cai, H. Zhang, Z. Liu, X. Bao, Reaction-induced strong metal–support interactions between metals and inert boron nitride nanosheets, *J. Am. Chem. Soc.* 142 (2020) 17167–17174.
- [25] A.M. Kovalskii, I.N. Volkov, N.D. Evdokimenko, O.P. Tkachenko, D.V. Leybo, I. V. Chepkasov, Z.I. Popov, A.T. Matveev, A. Manakhov, E.S. Permyakova, A. S. Konopatsky, A.L. Kustov, D.V. Golberg, D.V. Shtansky, Hexagonal BN- and BNO-supported Au and Pt nanocatalysts in carbon monoxide oxidation and carbon dioxide hydrogenation reactions, *Appl. Catal. B Environ.* 303 (2022), 120891.
- [26] S. Chen, R. Xu, J. Liu, X. Zou, L. Qiu, F. Kang, B. Liu, H.-M. Cheng, Simultaneous production and functionalization of boron nitride nanosheets by sugar-assisted mechanochemical exfoliation, *Adv. Mater.* 31 (2019), 1804810.
- [27] A.M. Love, B. Thomas, S.E. Specht, M.P. Hanrahan, J.M. Venegas, S.P. Burt, J. T. Grant, M.C. Cendejas, W.P. McDermott, A.J. Rossini, I. Hermans, Probing the transformation of boron nitride catalysts under oxidative dehydrogenation conditions, *J. Am. Chem. Soc.* 141 (2019) 182–190.
- [28] L. Zhou, P. Jiao, L. Fang, L. Liu, Z. Hao, H. Wang, Y.-M. Kang, K. Zhang, J. Chen, Two-phase transition induced amorphous metal phosphides enabling rapid, reversible alkali-metal ion storage, *ACS Nano* 15 (2021) 13486–13494.
- [29] H. Liu, J. Guan, S. Yang, Y. Yu, R. Shao, Z. Zhang, M. Dou, F. Wang, Q. Xu, Metal–organic framework-derived Co₂P nanoparticle/multi-doped porous carbon as a trifunctional electrocatalyst, *Adv. Mater.* 32 (2020), 2003649.
- [30] L. Yang, J. Feng, Z. Liu, Y. Duan, S. Zhan, S. Yang, K. He, Y. Li, Y. Zhou, N. Yuan, J. Ding, S. Liu, Record-efficiency flexible perovskite solar cells enabled by multifunctional organic ions interface passivation, *Adv. Mater.* (2022), <https://doi.org/10.1002/adma.202201681>.
- [31] Z. Chen, X. Zeng, X. Li, Z. Lv, J. Li, Y. Zhang, Strong metal phosphide–phosphate support interaction for enhanced non-noble metal catalysis, *Adv. Mater.* 34 (2022), 2106724.
- [32] H. Wang, L. Wang, D. Lin, X. Feng, Y. Niu, B. Zhang, F.-S. Xiao, Strong metal–support interactions on gold nanoparticle catalysts achieved through Le Chatelier's principle, *Nat. Catal.* 4 (2021) 418–424.
- [33] P. Wu, L. Lu, J. He, L. Chen, Y. Chao, M. He, F. Zhu, X. Chu, H. Li, W. Zhu, Hexagonal boron nitride: a metal-free catalyst for deep oxidative desulfurization of fuel oils, *Green Energy Environ.* 5 (2020) 166–172.

- [34] G. Zhou, M. Li, Y. Li, H. Dong, D. Sun, X. Liu, L. Xu, Z. Tian, Y. Tang, Regulating the electronic structure of CoP nanosheets by O incorporation for high-efficiency electrochemical overall water splitting, *Adv. Funct. Mater.* 30 (2020), 1905252.
- [35] Y. Pan, K. Sun, S. Liu, X. Cao, K. Wu, W.-C. Cheong, Z. Chen, Y. Wang, Y. Li, Y. Liu, D. Wang, Q. Peng, C. Chen, Y. Li, Core-shell ZIF-8@ZIF-67-derived CoP nanoparticle-embedded N-doped carbon nanotube hollow polyhedron for efficient overall water splitting, *J. Am. Chem. Soc.* 140 (2018) 2610–2618.
- [36] T. Wang, Y. Jiang, Y. Zhou, Y. Du, C. Wang, In situ electrodeposition of CoP nanoparticles on carbon nanomaterial doped polyphenylene sulfide flexible electrode for electrochemical hydrogen evolution, *Appl. Surf. Sci.* 442 (2018) 1–11.
- [37] Z. Huang, Z. Chen, Z. Chen, C. Lv, M.G. Humphrey, C. Zhang, Cobalt phosphide nanorods as an efficient electrocatalyst for the hydrogen evolution reaction, *Nano Energy* 9 (2014) 373–382.
- [38] T.-S. Kim, H.J. Song, J.-C. Kim, B. Ju, D.-W. Kim, 3D architectures of Co_xP using silk fibroin scaffolds: an active and stable electrocatalyst for hydrogen generation in acidic and alkaline media, *Small* 14 (2018), 1801284.
- [39] T. Liu, J. Mou, Z. Wu, C. Lv, J. Huang, M. Liu, A facile and scalable strategy for fabrication of superior bifunctional freestanding air electrodes for flexible zinc–air batteries, *Adv. Funct. Mater.* 30 (2020), 2003407.
- [40] M. Fan, J.D. Jimenez, S.N. Shirodkar, J. Wu, S. Chen, L. Song, M.M. Royko, J. Zhang, H. Guo, J. Cui, K. Zuo, W. Wang, C. Zhang, F. Yuan, R. Vajtai, J. Qian, J. Yang, B.I. Yakobson, J.M. Tour, J. Lauterbach, D. Sun, P.M. Ajayan, Atomic Ru immobilized on porous h-BN through simple vacuum filtration for highly active and selective CO₂ methanation, *ACS Catal.* 9 (2019) 10077–10086.
- [41] W.-D. Oh, Z. Wong, X. Chen, K.-Y.A. Lin, A. Veksha, G. Lisak, C. He, T.-T. Lim, Enhanced activation of peroxydisulfate by CuO decorated on hexagonal boron nitride for bisphenol a removal, *Chem. Eng. J.* 39 (2020), 124714.
- [42] Z. He, C. Kim, L. Lin, T.H. Jeon, S. Lin, X. Wang, W. Choi, Formation of heterostructures via direct growth CN on h-BN porous nanosheets for metal-free photocatalysis, *Nano Energy* 42 (2017) 58–68.
- [43] Z. Huang, W. Zhao, Coupling hybrid of HBN nanosheets and TiO₂ to enhance the mechanical and tribological properties of composite coatings, *Prog. Org. Coat.* 148 (2020), 105881.
- [44] H. Liu, Y. Liu, S. Mehdi, X. Wu, T. Liu, B. Zhou, P. Zhang, J. Jiang, B. Li, Surface phosphorus-induced CoO coupling to monolithic carbon for efficient air electrode of quasi-solid-state Zn-air batteries, *Adv. Sci.* 8 (2021), 2101314.
- [45] R. Shen, Y. Liu, H. Wen, T. Liu, Z. Peng, X. Wu, X. Ge, S. Mehdi, H. Cao, E. Liang, J. Jiang, B. Li, Engineering V₂O₅-Ti ensemble to boost the activity of Ru towards water dissociation for catalytic hydrogen generation, *Appl. Catal. B Environ.* 306 (2022), 121100.
- [46] Y. Lin, L. Yang, Y. Zhang, H. Jiang, Z. Xiao, C. Wu, G. Zhang, J. Jiang, L. Song, Defective carbon-CoP nanoparticles hybrids with interfacial charges polarization for efficient bifunctional oxygen electrocatalysis, *Adv. Energy Mater.* 8 (2018), 1703623.
- [47] X. Duan, J. Kang, W. Tian, H. Zhang, S.-H. Ho, Y.-A. Zhu, Z. Ao, H. Sun, S. Wang, Interfacial-engineered cobalt@carbon hybrids for synergistically boosted evolution of sulfate radicals toward green oxidation, *Appl. Catal. B Environ.* 256 (2019), 117795.
- [48] H. Zhang, K. Zhang, S. Ashraf, Y. Fan, S. Guan, X. Wu, Y. Liu, B. Liu, B. Li, Polar O-Co-P surface for bimolecular activation in catalytic hydrogen generation, *Energy Environ. Mater.* (2021), <https://doi.org/10.1002/eeem2.12273>.
- [49] Y. Chen, J. Cai, P. Li, G. Zhao, G. Wang, Y. Jiang, J. Chen, S.X. Dou, H. Pan, W. Sun, Hexagonal boron nitride as a multifunctional support for engineering efficient electrocatalysts toward the oxygen reduction reaction, *Nano Lett.* 20 (2020) 6807–6814.
- [50] Z. Gao, G. Wang, T. Lei, Z. Lv, M. Xiong, L. Wang, S. Xing, J. Ma, Z. Jiang, Y. Qin, Enhanced hydrogen generation by reverse spillover effects over bicomponent catalysts, *Nat. Commun.* 13 (2022) 118.